nature communications

Article

https://doi.org/10.1038/s41467-026-69719-z

Simultaneous promotion of photocatalytic CH_4 conversion and H_2O_2 production via nanopore water confinement

Received: 15 June 2025

Accepted: 9 February 2026

Published online: 17 February 2026

Check for updates

Fanxun Lv[1], Shengwei Wei[1], Xiaoyan Wu[1], Chenghang Qi[1], Xuan Wang[1], Xiaoning Liu[1], Yi Yu[1,2], Bo Yang[1] ✉ & Chenlu Xie[1,2] ✉

Aqueous photocatalytic CH_4 oxidation offers a promising route for converting natural gas into oxygenates, a process governed by multi-electron and proton transfer at the catalyst-water interface. Here, we demonstrate that spatially confining water within Au/TiO_2@pSiO_2 core-shell catalysts—by reducing silica pore size to 1.7 nm—increases CH_4 conversion three-fold and H_2O_2 production 22-fold compared to Au/TiO_2. This strategy is generalizable to other semiconductors and cocatalysts, with Pt/TiO_2@pSiO_2-1.7 exhibiting oxygenate yields of 32.7 mmol g^{-1} h^{-1} and a 14.1% apparent quantum yield at 365 nm. Spectroscopic studies and molecular dynamics simulations reveal that water confined within pores, with a weakened hydrogen-bonding network, alters proton-coupled electron transfer pathways. Water oxidation transits to a concerted pathway, favoring •OH production for CH_4 conversion, while oxygen reduction shifts to a two-electron process, directly producing H_2O_2. This work highlights the potential of water confinement for designing efficient photocatalysts for CH_4 conversion.

Aqueous photochemical processes are vital for energy conversion and environmental applications, such as water splitting[1], O_2/CO_2 reduction[2], and pollutants removal[3]. These processes typically involve multi-electron and multi-proton transfer steps that generate reactive oxygen species (ROS) as key intermediates[3–5]. Photocatalytic methane oxidation has emerged as a green route to directly transform abundant natural gas into valuable fuels and chemicals, such as methanol[6–8]. This approach utilizes photon energy to overcome the high activation barriers of CH_4, enabling room-temperature conversion via hydroxyl radicals (•OH) and bypassing the energy-intensive syngas route[6,9]. Moreover, the aqueous environment offers unique advantages in improving product selectivity by facilitating the desorption of partially oxygenated products[9,10]. Although extensive research has focused on developing photocatalysts with enhanced charge separation and surface reactions regulation through band structure engineering[11–13] and cocatalyst modification[9,14–18], the potential of tuning the aqueous microenvironment surrounding the semiconductor to boost CH_4 conversion remains largely unexploited.

Aqueous photocatalytic CH_4 oxidation involves a complex network of electron transfer (ET) and proton transfer (PT) reactions at the semiconductor-water interface (Fig. 1, Supplementary Fig. 1), where water serves as a reactant, proton source, and solvent[19–21]. For hydrophilic oxide semiconductors like TiO_2, water is the primary hole acceptor, generating •OH via proton and electron transfer (Fig. 1a)[9,20]. These •OH radicals activate CH_4 through hydrogen atom transfer (HAT), forming methyl radicals (•CH_3). Simultaneously, O_2 is reduced to superoxide radicals (•OOH), which further contribute to •CH_3 conversion into oxygenates[15]. These ET and PT events can occur stepwise or concertedly via proton-coupled electron transfer (PCET) mechanisms, which are highly sensitive to the solvent environment due to the significant energy required for solvent reorganization—especially in water[22,23]. While studies over model reactions have shown examples of enhanced catalytic performance by tuning water structure[24–33], its

[1]School of Physical Science and Technology, ShanghaiTech University, Shanghai, China. [2]Shanghai Key Laboratory of High-Resolution Electron Microscopy, ShanghaiTech University, Shanghai, China. ✉e-mail: yangbo1@shanghaitech.edu.cn; xiechl@shanghaitech.edu.cn

https://doi.org/10.1038/s41467-026-69719-z

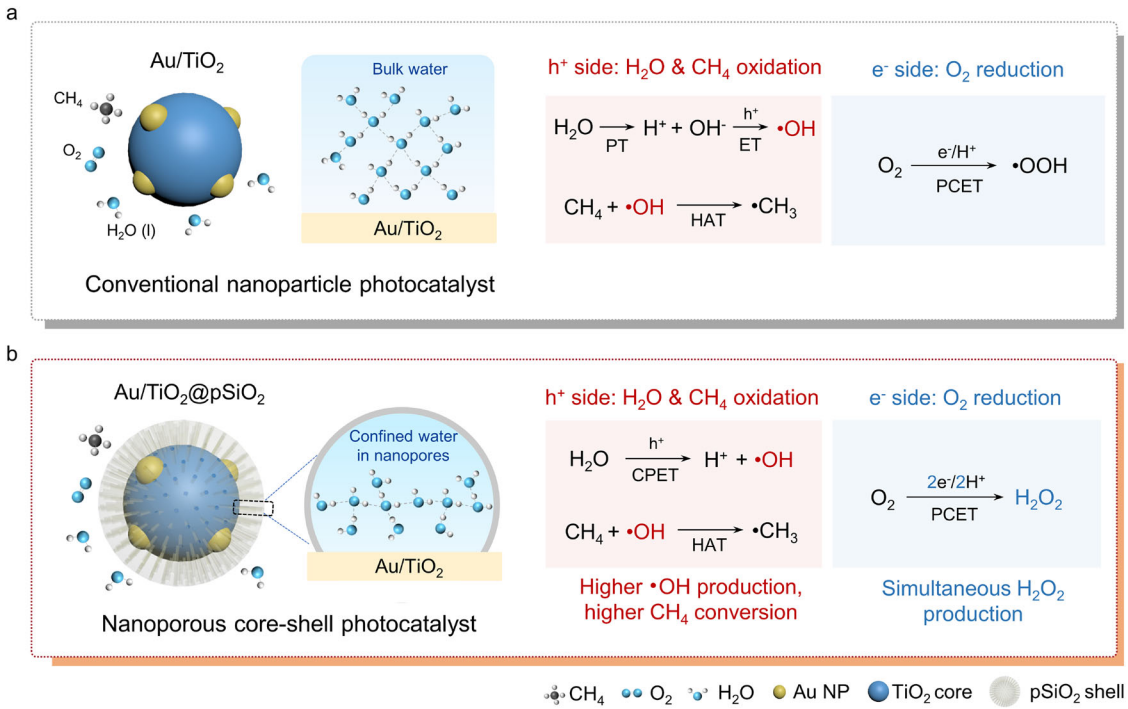

Fig. 1 | Design of nanoporous core-shell photocatalyst for enhanced CH_4 conversion and simultaneous H_2O_2 production. a Schematic representation of PCET and CH_4 activation pathways in photocatalytic CH_4 oxidation over Au/TiO_2 in bulk water. **b** Schematic representation of PCET and CH_4 activation pathways in photocatalytic CH_4 oxidation over $Au/TiO_2@pSiO_2$ with confined water. The black dashed rectangle and blue dashed lines show a schematic of the disrupted water structure inside the nanopore. In (**a**, **b**), colored spheres represent specific atoms (light gray: H; dark gray: C; ice blue: O). PT: proton transfer; ET: electron transfer; PCET: proton-coupled electron transfer; CPET: concerted proton-electron transfer; HAT: hydrogen atom transfer; h^+: holes; e^-: electrons.

application to complex photocatalytic reactions such as methane oxidation remains largely unexplored. Therefore, designing a photocatalyst that modulates water structure near the semiconductor interface presents a promising avenue for tuning proton/electron transfer pathways and optimizing methane oxidation kinetics.

Spatial confinement via tunable nanopores offers an effective strategy to alter water structure[22,34], and consequently, the dynamics of these ET and PT processes[35]. Confined water is known to exhibit distinct hydrogen-bonding (HB) networks, physical properties and reactivities compared to bulk water[35,36]. In this work, we demonstrate that water confinement by silica nanopores in $Au/TiO_2@pSiO_2$ catalysts modulates PCET pathways and achieves efficient CH_4 conversion and H_2O_2 production simultaneously (Fig. 1b). We select TiO_2 as the semiconductor material for its ability to oxidize water to •OH radicals[12,20] and employ a noble metal cocatalyst to enhance CH_4 conversion[9,14,37]. Water confinement is achieved by installing nanoporous and UV-transparent SiO_2 enclosures on the Au/TiO_2 core. Reducing the silica pore size from 3.1 nm to 1.7 nm leads to an approximately three-fold enhancement in CH_4 conversion and a 22-fold increase in H_2O_2 production compared to Au/TiO_2. This confinement strategy is applicable to other metal cocatalysts and semiconductors, as demonstrated by $Pt/TiO_2@pSiO_2$-1.7, achieving maximum oxygenate yields of 32.7 mmol g^{-1} h^{-1} with 95.5% selectivity and an apparent quantum yield (AQY) of 14.1% at 365 nm. Mechanistic investigations and molecular dynamics (MD) simulations with machine learning potentials (MLPs) reveal that the weakened HB network of confined water modulates PCET pathways for both water oxidation reaction (WOR) and oxygen reduction reaction (ORR). Specifically, WOR shifts from stepwise to concerted PCET, enhancing •OH radical production for CH_4 conversion, while ORR shifts from a one-electron ($1e^-$) to a $2e^-$ process, promoting H_2O_2 production. These findings underscore the potential of engineering water structures via spatial confinement to promote photocatalytic activity and selectivity.

Results

Synthesis and characterization of $Au/TiO_2@pSiO_2$ catalysts

TiO_2 is a well-established semiconductor for photocatalytic methane oxidation, with a valence band position sufficient for oxidizing water to •OH radicals[12,20]. Noble metal cocatalyst modification is known to promote CH_4 conversion[9,14,37]. Therefore, we selected Au/TiO_2 as the model catalyst to study the effect of water confinement. We chose the SiO_2 enclosure due to its facile growth, controllable pore size, optical transparency in the UV region, and good stability. Furthermore, our previous studies have shown that a thin, non-porous silica shell can prevent oxygenates overoxidation while still allowing •OH radicals transport and convert CH_4[20], indicating good compatibility of silica with the TiO_2-based photocatalysts.

Gold nanoparticles (NPs) were loaded onto TiO_2 (P25) via $NaBH_4$ reduction[9,38], and a nanoporous silica shell was constructed on Au/TiO_2 using the Stöber method with alkylammonium surfactants as templates (Fig. 2a)[39]. By varying surfactant carbon chain length or adding auxiliary organics[40,41], we obtained $Au/TiO_2@pSiO_2$-X with different pore sizes (X = pore size). The surface area and porosity of $Au/TiO_2@pSiO_2$-X were characterized by nitrogen physisorption (Fig. 2e, Supplementary Table 1). Using cetyltrimethylammonium bromide ($C_{16}TAB$) resulted in mesopores ~2.6 nm, while a shorter surfactant, dodecyltrimethylammonium bromide ($C_{12}TAB$), yielded smaller pores around 1.7 nm (Fig. 2f). Adding hexane as a pore-expanding agent yielded larger pores around 3.1 nm. For comparison, $Au/TiO_2@SiO_2$ without nanopores were synthesized similarly but without alkylammonium surfactants (Supplementary Fig. 2).

Transmission electron microscopy (TEM), energy-dispersive X-ray spectroscopy (EDS), and X-ray diffraction (XRD) confirmed full encapsulation of Au/TiO_2 by a uniform, amorphous SiO_2 shell across all $Au/TiO_2@pSiO_2$-X catalysts (Fig. 2b–d, Supplementary Figs. 3–5). The silica layer had an average thickness of 8 nm (Fig. 2b–d), which is tunable by varying the amount of tetraethyl orthosilicate (TEOS)

https://doi.org/10.1038/s41467-026-69719-z

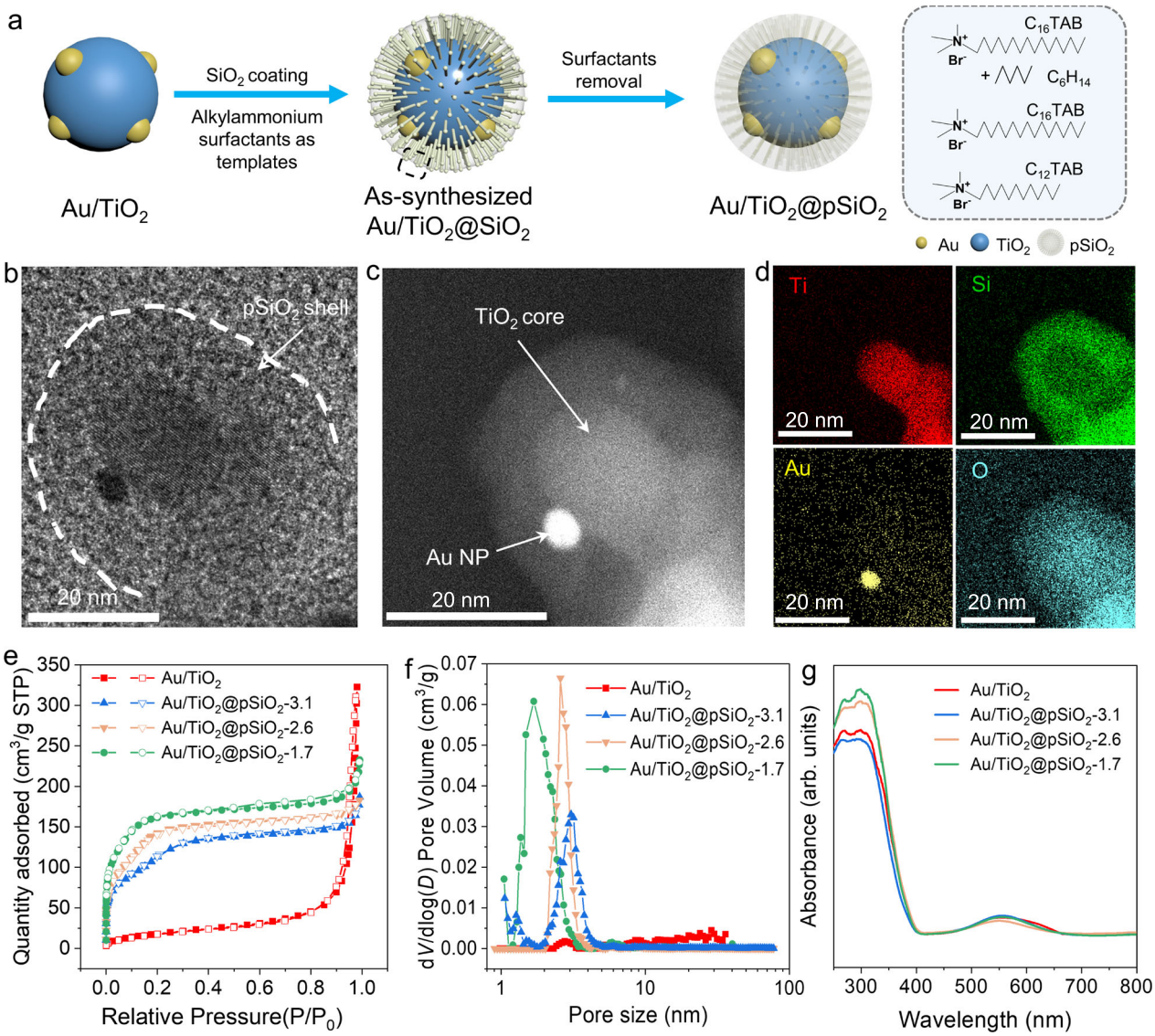

Fig. 2 | Structural characterizations of Au/TiO2@pSiO2 with varying silica pore sizes. a Schematic illustration of the preparation of $Au/TiO_2@pSiO_2$-X catalysts. The black dashed box highlights the template agents used in material synthesis: $C_{12}TAB$, dodecyltrimethylammonium bromide; $C_{16}TAB$, cetyltrimethylammonium bromide. **b** HR-TEM image of $Au/TiO_2@pSiO_2$-1.7 catalysts. The white dashed line outlines the porous SiO_2 shell, and the white arrow points to the SiO_2 shell. **c** A High-angle annular dark-field scanning transmission electron microscopy (HAADF-STEM) image of $Au/TiO_2@pSiO_2$-1.7 catalysts. White arrows point to the highly dispersed Au NP and TiO_2 core, respectively. **d** EDS mapping images of $Au/TiO_2@pSiO_2$-1.7. Different colors correspond to different elements (red: Ti; green: Si; yellow: Au; cyan: O). **e** N_2 adsorption-desorption isotherms of Au/TiO_2 and $Au/TiO_2@pSiO_2$-X. **f** Pore size distribution of Au/TiO_2 and $Au/TiO_2@pSiO_2$-X. **g** UV-Vis DRS of Au/TiO_2 and $Au/TiO_2@pSiO_2$-X.

(Supplementary Fig. 6). Au NPs ranging 2–6 nm were randomly dispersed on TiO_2 (Fig. 2b–d, Supplementary Fig. 3), with a loading of ~0.1 wt% (Supplementary Table 2). Contact angle measurements demonstrate that catalysts with different pore sizes exhibit similar hydrophilic properties (Supplementary Fig. 7). UV-visible diffusive reflective spectra (UV-Vis DRS) of Au/TiO_2 and $Au/TiO_2@pSiO_2$-X were nearly identical (Fig. 2g, Supplementary Fig. 8), suggesting minimal effect of the SiO_2 coating on light absorption. X-ray photoelectron spectra (XPS) showed similar Ti oxidation states among all samples (Supplementary Fig. 9). These results indicate that the nanoporous coating does not significantly modify the intrinsic properties of the semiconductors.

Pore-size dependent CH_4 photocatalytic oxidation by $Au/TiO_2@pSiO_2$-X

Photocatalytic reactions were conducted in a batch reactor with 100 mL of distilled water under 2.5 MPa CH_4 and 1 MPa O_2 at 25 °C (Supplementary Fig. 10). Liquid products (CH_3OOH, CH_3OH, and HCOOH) were analyzed by ^{1}H-NMR, while HCHO was quantified by colorimetry methods (Supplementary Fig. 11). Control experiments, including dark and catalyst-free controls (Supplementary Table 3), and a $^{13}CH_4$ isotope-labeling study (Supplementary Fig. 12), validated that oxygenates were generated from photocatalytic methane oxidation over $Au/TiO_2@pSiO_2$. Compared to bare Au/TiO_2, $Au/TiO_2@pSiO_2$ significantly enhanced oxygenate yields, which increased as pore size decreased (Fig. 3a, b). $Au/TiO_2@pSiO_2$-3.1 exhibited a total oxygenates yield of 18.0 ± 0.4 mmol g^{-1} h^{-1}, with 92.5% selectivity. Further reducing the pore size to 1.7 nm led to higher yields, achieving 27.4 ± 0.6 mmol g^{-1} h^{-1}—approximately triple that of Au/TiO_2. The AQY for $Au/TiO_2@pSiO_2$-1.7 was 10.9 ± 0.3% at 365 nm (Supplementary Fig. 13, Supplementary Table 4), substantially exceeding Au/TiO_2 (3.3 ± 0.2%). Furthermore, this performance trend remained consistent under a broad-spectrum Xenon lamp, demonstrating that the catalytic improvement is independent of the specific light source

https://doi.org/10.1038/s41467-026-69719-z

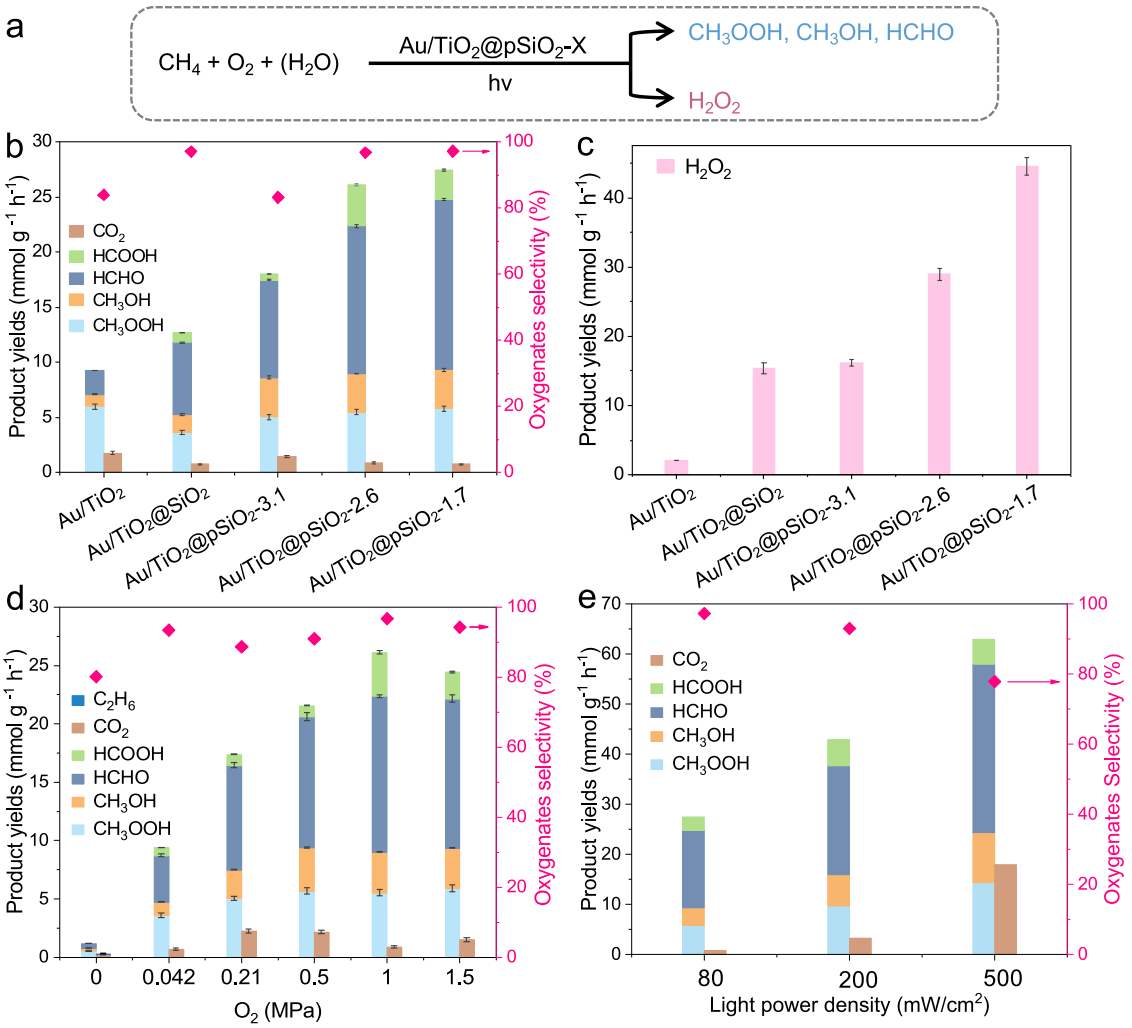

Fig. 3 | Photocatalytic performance for methane oxidation. a Schematics of products formation from CH_4 and O_2 over Au/TiO_2@pSiO_2-X. **b** Yields of oxygenates from CH_4 oxidation over different photocatalysts. **c** H_2O_2 production over different photocatalysts. Reaction conditions for (**b**, **c**): 10 mg catalysts, 100 mL H_2O, 2.5 MPa CH_4, 1 MPa O_2, 1 h reaction time, reaction temperature of 25 ± 3 °C, light source of 365 nm UV LED, 80 mW/cm^2. **d** O_2 partial pressure dependence on Au/TiO_2@pSiO_2-2.6. Reaction conditions: 10 mg catalysts, 100 mL H_2O, 2.5 MPa CH_4, 1 h reaction time, reaction temperature of 25 ± 3 °C, light source of 365 nm UV LED, 80 mW/cm^2. **e** Productivity assessment of Au/TiO_2@pSiO_2-1.7 obtained at different light intensities. Reaction conditions: 10 mg catalysts, 100 mL H_2O, 2.5 MPa CH_4, 1 MPa O_2, 1 h reaction time, reaction temperature of 25 ± 3 °C, light source of 365 nm UV LED. In (**b**–**e**), bars represent product yields (left y-axis), while the pink diamonds and corresponding pink arrow indicate oxygenate selectivity (right y-axis). The error bars in (**b**–**d**) represent the standard deviations derived from three independent experiments.

(Supplementary Fig. 14). Notably, Au/TiO_2@pSiO_2 also produced a significant amount of H_2O_2 as a valuable byproduct (Fig. 3a, c, Supplementary Figs. 15–17 and Supplementary Note 1). The H_2O_2 production also increased with decreasing pore size, reaching 44.6 ± 1.3 mmol g^{-1} h^{-1} for Au/TiO_2@pSiO_2-1.7 (Fig. 3c), representing a 22-fold increase over Au/TiO_2 and competitive with state-of-the-art catalysts (Supplementary Table 5).

Further optimization of parameters, including light intensity, water volume, and Au loading, was performed (Fig. 3e, Supplementary Figs. 18, 19). By increasing the light flux to 500 mW/cm^2, we achieved a yield of 62.9 mmol g^{-1} h^{-1} with 80% selectivity for oxygenates (Fig. 3e). Au/TiO_2@pSiO_2-1.7 remained stable over ten cycles, with consistent production and selectivity (Supplementary Fig. 20). XRD and TEM showed no obvious structure changes in the spent catalyst (Supplementary Fig. 21), and N_2 adsorption isotherms showed pore size distribution and surface area similar to those of fresh catalysts (Supplementary Fig. 22). ICP-OES analysis verified that the gold loading remained unchanged after cycles, with negligible gold leaching observed (Supplementary Table 6).

To elucidate the role of the nanoporous silica shell, a series of control experiments was performed. A physical mixture of Au/TiO_2 and porous SiO_2 (pSiO_2-1.7) showed similar catalytic performance to Au/TiO_2 alone, highlighting the importance of the core-shell architecture (Supplementary Figs. 23, 24). Notably, Au/TiO_2@SiO_2 without pores yielded more than Au/TiO_2 but less than the nanoporous catalysts (Fig. 3b), probably due to the greater diffusion barrier in nonporous silica. This trend signifies the importance of controlling silica pore size for efficient methane conversion.

Silica thickness also significantly impacts performance, showing a non-monotonic effect. For Au/TiO_2@pSiO_2 catalysts with an identical pore size and surface hydrophilicity, an 8 nm shell was optimal (Supplementary Figs. 6, 25–27). A 30 nm shell reduced yields (Supplementary Fig. 27), likely due to an increased diffusion barrier. However, thinner shells (3.6 nm and 6 nm) also resulted in lower yields; the catalyst with a 3.6 nm shell, in particular, was substantially less active. This is likely attributed to an ultra-thin shell failing to provide complete and uniform encapsulation over TiO_2, thus being unable to establish an effective water confinement environment. These findings reveal a

critical trade-off: the shell must be thick enough to create an effective confined microenvironment but thin enough to minimize mass transport resistance. Thus, a shell architecture with both optimal porosity and thickness is essential.

Given the critical role of the nanoporous shell, we investigated its influence on gaseous reactant transport. Temperature-programmed desorption of CH_4 (CH_4-TPD) showed weak adsorption on both Au/TiO_2 and Au/TiO_2@pSiO_2-1.7 (Supplementary Fig. 28), with the latter showing an even lower adsorption temperature. These results rule out CH_4 enrichment as the source of improved catalytic performance. We then examined the effect of O_2, whose direct participation in oxygenates formation was confirmed by ^{18}O isotopic labeling (Supplementary Fig. 29). Both Au/TiO_2 and Au/TiO_2@pSiO_2-X exhibited low yield under anaerobic conditions, with yields increasing with O_2 pressure (Fig. 3d, Supplementary Fig. 30). Au/TiO_2 achieved maximum yield at 0.042 MPa O_2, whereas Au/TiO_2@pSiO_2-2.6 and Au/TiO_2@pSiO_2-1.7 required higher pressures (up to 1 MPa), suggesting hindered O_2 transport by the silica shell (Fig. 3d, Supplementary Fig. 30a, b and Supplementary Note 2). Furthermore, TiO_2 and TiO_2@pSiO_2 required higher O_2 pressures to attain optimal yields compared to their Au-incorporated counterparts (Supplementary Fig. 30c, d), and relocating Au NPs to the SiO_2 surface decreased product yields (Supplementary Fig. 31). These results indicate that the enhanced performance of Au/TiO_2@pSiO_2 is not due to O_2 enrichment from its high surface area. Instead, O_2 transport within silica shell is hindered in aqueous solution; however, the adverse effect of limited O_2 transport on overall product yield is mitigated by a combination of increasing O_2 pressure and effective O_2 utilization enabled by the supported Au cocatalysts. The function of Au as an electron acceptor for O_2 reduction was confirmed using in situ XPS, where the Au 4*f* signal shifted to lower binding energies upon illumination (Supplementary Fig. 32).

The counter-intuitive observation that the SiO_2 shell promotes catalytic performance despite impeding O_2 transport implies the enhancement originates not from gaseous reactant enrichment. We therefore hypothesized that the origin is the confinement of water layers within the hydrophilic nanopores. To further decouple these factors, we systematically modified the optimal Au/TiO_2@pSiO_2-1.7 catalyst with methyltrimethoxysilane (MTMS) to increase its surface hydrophobicity while preserving the pore structure (Supplementary Figs. 33–36). Fourier transform infrared (FTIR) spectra confirmed the successful surface grafting (Supplementary Fig. 37). At low modification levels (e.g., 0.1–0.5 wt%), the shell thickness, pore size, and surface area of the catalyst remained unchanged (Supplementary Figs. 33, 34), while a higher 5% MTMS loading caused a decrease in surface area, likely attributed to pore blockage. In principle, a more hydrophobic surface is expected to enrich nonpolar reactants like CH_4 and O_2 and potentially accelerate the reaction[42–44]. However, the catalytic results show the opposite trend: oxygenate yields decreased drastically compared to the unmodified, hydrophilic catalyst (Supplementary Fig. 36). Even a tiny 0.1 wt% MTMS modification, corresponding to an estimated Si–CH_3 surface coverage of <0.5% (Supplementary Table 7), was sufficient to significantly suppress the reaction. This extreme sensitivity to a miniscule fraction of hydrophobic groups provides strong evidence that the interfacial water environment, rather than the mass transport of gaseous reactants, plays the dominant role in the catalytic enhancement.

Generalization of the nanoporous confinement strategy

We explored this confinement strategy with different metal cocatalysts and semiconductors. Substituting Au with Pd, Pt, or Rh exhibited a similar trend: confined pores around metal-TiO_2 surface significantly promoted oxygenates and H_2O_2 yields compared to bare metal-TiO_2 catalysts, with smaller pores yielding higher productions (Fig. 4a, Supplementary Figs. 38, 39 and Supplementary Note 3). Among these, Pt/TiO_2@pSiO_2-1.7 achieved oxygenate yields of 32.7 ± 0.8 mmol g^{-1} h^{-1}

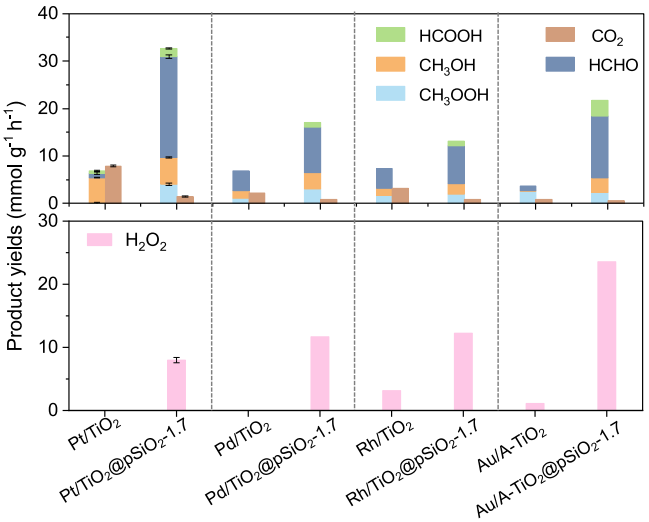

Fig. 4 | Generalization of the photocatalyst confinement strategy. Yields of oxygenated product and H_2O_2 from photocatalytic methane oxidation over core-shell photocatalysts with different metal cocatalysts and semiconductors. Reaction conditions: 10 mg catalysts, 100 mL H_2O, 2.5 MPa CH_4, 1 MPa O_2, 1 h reaction time, reaction temperature of 25 ± 3 °C, light source: 365 nm UV LED, 80 mW/cm^2. The error bars represent the standard deviations derived from three independent experiments. The vertical dashed lines categorize the different cocatalysts and semiconductor supports.

and an AQY of 14.1 ± 0.3% for CH_4 oxidation at 365 nm, representing competitive performance relative to previously reported catalysts (Fig. 4, Supplementary Tables 4, 8). We further extended our study to other semiconductors, including $BiVO_4$, ZnO and anatase TiO_2 (A-TiO_2) (Fig. 4a, Supplementary Figs. 40–42 and Supplementary Note 3). Applying the porous silica coating improved oxygenate yields and H_2O_2 production for these catalysts. For example, Au/A-TiO_2@pSiO_2-1.7 achieved oxygenate and H_2O_2 formation rates approximately 5 and 21 times higher than those of Au/A-TiO_2, respectively (Fig. 4a). These results underscore the versatility of the nanoporous confinement design, demonstrating its broad applicability across different photocatalyst systems.

Key ROS for photocatalytic CH_4 oxidation

We also investigated the role of SiO_2 shell in photocarrier separation using photoluminescence (PL) and photocurrent measurements, and electrochemical impedance spectroscopy (EIS). Steady-state and time-resolved PL (TRPL) spectroscopy revealed that the silica shell has a negligible impact on photocarrier separation and lifetimes (Supplementary Figs. 43, 44). Furthermore, Au/TiO_2 showed a higher photocurrent and lower impedance compared to Au/TiO_2@pSiO_2 (Supplementary Figs. 45, 46). These results, together with findings on gas transport and surface modifications (Supplementary Note 2), demonstrate that improved performance in Au/TiO_2@pSiO_2 is not due to improved photocarrier separation or gas transport, but rather to effects associated with the structure of the confined water layers in contact with the semiconductors.

To unravel the underlying mechanism, we next sought to identify the key ROS responsible for methane activation and H_2O_2 formation within the confined environment. This can be achieved by introducing sacrificial agents that selectively quench different ROS and monitor the change in methane conversion[15,45]. Both holes and •OH radicals are capable of activating methane[9,14,15]. We used salicylic acid and $(NH_4)_2C_2O_4$ to scavenge •OH radicals and holes (h^+), respectively[15]. The addition of salicylic acid nearly completely inhibited CH_4 conversion, showing a stronger suppression than $(NH_4)_2C_2O_4$ (Supplementary

https://doi.org/10.1038/s41467-026-69719-z

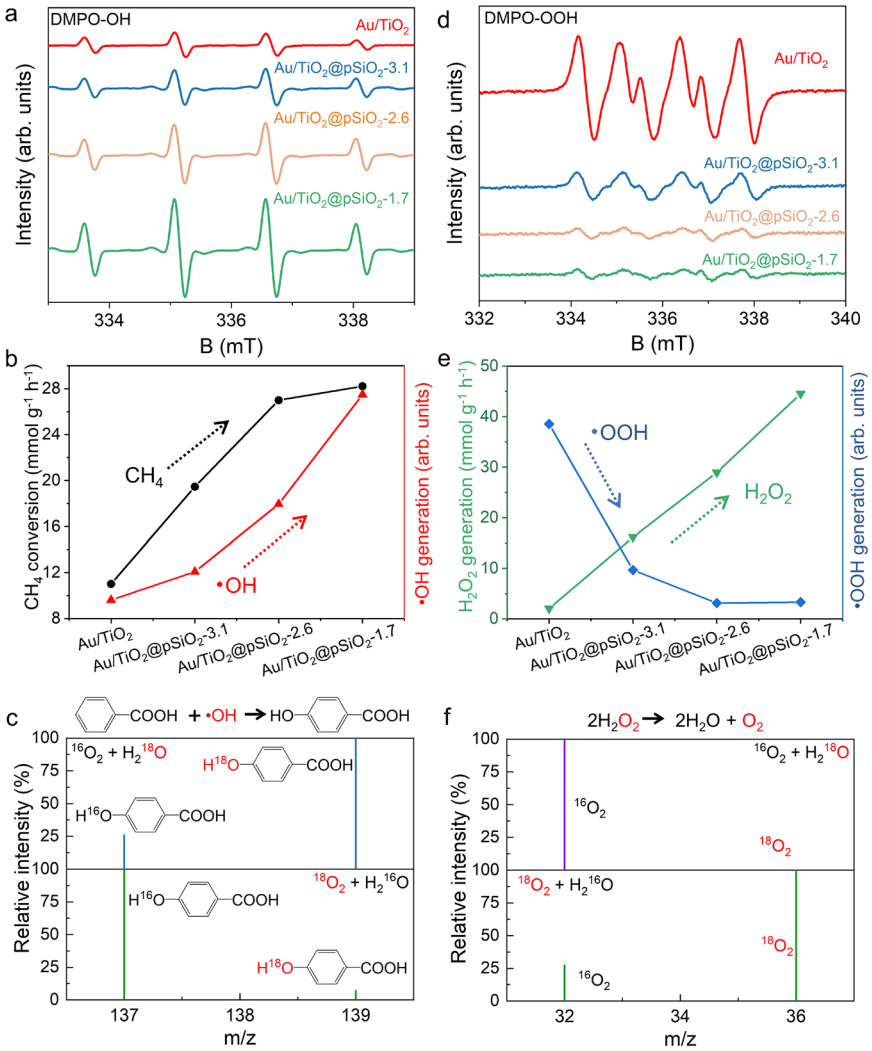

Fig. 5 | Key ROS detection for photocatalytic CH4 oxidation. a In situ EPR spectra of DMPO-OH for monitoring the generation of •OH radicals over Au/TiO_2 and $Au/TiO_2@pSiO_2$-X. **b** Correlation between CH_4 conversion rate with •OH radical production rate over different photocatalysts. Black and red arrows denote the trends in methane conversion and •OH generation versus pore size, respectively. **c** ^{18}O isotopic studies on the origins of •OH radicals over $Au/TiO_2@pSiO_2$-1.7, with benzoic acid used as a probe to capture •OH in situ. **d** In situ EPR spectra of DMPO-OOH for monitoring the generation of •OOH active species over Au/TiO_2 and $Au/TiO_2@pSiO_2$-X. **e** Correlation between H_2O_2 generation and •OOH radical production rate over different photocatalysts. Blue and green arrows denote the trends in •OOH and H_2O_2 generation versus pore size. **f** ^{18}O isotopic studies on the origins of H_2O_2 over $Au/TiO_2@pSiO_2$-1.7.

Fig. 47). This suggests that •OH radicals, rather than h^+, are the main reactive species for CH_4 activation.

The $Au/TiO_2@pSiO_2$ catalyst with smaller pores produced more •OH radicals, as monitored by in situ electron paramagnetic resonance (EPR), which correlates with their increased performance in CH_4 conversion (Fig. 5a, b). Coumarin was also employed as a fluorescent probe to assess •OH production[15], which further supports the findings from EPR (Supplementary Figs. 48, 49). Typically, there are two distinct pathways by which •OH radicals are formed: one involves H_2O oxidation by holes ($1e^-$ WOR), while the other involves O_2 reduction by electrons (ORR) (Supplementary Fig. 1). To identify its origin, we performed ^{18}O isotopic labeling with benzoic acid as a probe to capture •OH (Supplementary Fig. 50). Under $H_2{}^{16}O/{}^{18}O_2$ conditions, over 95% of products corresponded to $H^{16}OC_6H_4CO_2H$ (m/z = 137), while with $H_2{}^{18}O/{}^{16}O_2$, approximately 80% of products corresponded to $H^{18}OC_6H_4CO_2H$ (m/z = 139). This revealed that •OH radicals primarily originate from $1e^-$ WOR rather than from O_2 reduction over $Au/TiO_2@pSiO_2$-1.7 (Fig. 5c, Supplementary Fig. 51). In contrast, for Au/TiO_2 and TiO_2, approximately half of the •OH radicals derive from H_2O oxidation and the other half from O_2 reduction (Supplementary Figs. 52, 53). Thus, the enhanced $1e^-$ WOR to •OH radicals within confined SiO_2 pores are responsible for the improved CH_4 conversion over $Au/TiO_2@pSiO_2$.

EPR spectra of DMPO-OOH show that $Au/TiO_2@pSiO_2$ with smaller pores produced less •OOH radicals (Fig. 5d), consistent with their enhanced H_2O_2 production as the main product in ORR (Fig. 5e). Electron scavenger experiments using $AgNO_3$ or $NaIO_3$ and $^{18}O_2/H_2{}^{18}O$ isotope labeling confirmed that H_2O_2 is generated exclusively through ORR (Fig. 5f, Supplementary Figs. 54, 55). The ORR selectivity to H_2O_2 is 75 % over $Au/TiO_2@pSiO_2$-1.7, compared to 11% over Au/TiO_2 (Supplementary Fig. 13, Supplementary Note 4). The high H_2O_2 production and negligible •OOH production over $Au/TiO_2@pSiO_2$ suggest that the silica nanopores confinement alters the ORR pathway from a $1e^-$ process to a $2e^-$ process.

Thus, facilitated $1e^-$ WOR producing •OH and an altered ORR pathway account for the improved catalytic performance of $Au/TiO_2@pSiO_2$. Similar enhancements in •OH production from $1e^-$ WOR and altered ORR pathways were also observed with $Pt/TiO_2@pSiO_2$ (Supplementary Figs. 56–58, Supplementary Note 3). These results indicate that this alteration is a general phenomenon when water is

spatially confined within nanopores. We hypothesize that both the accelerated 1e⁻ WOR and the modified ORR pathway result from the distinct structure of water confined within these nanopores compared to bulk water.

KIE investigations for CH_4 oxidation process

H/D kinetic isotope effect (KIE) studies were used to analyze whether PT is involved in the rate-determining step (RDS)[46–48], which would further shed light on the mechanism of altered reactivity and selectivity. For the 1e⁻ WOR that produces •OH radicals, Au/TiO_2@pSiO_2–1.7 shows a pronounced KIE value of 2.0–2.3, indicating a strong involvement of PT in the RDS. In contrast, Au/TiO_2 exhibits a low KIE value of 1.1–1.2 (Fig. 6a, Supplementary Figs. 59, 60), suggesting a distinctly different 1e⁻ WOR pathway. The absence of KIE for Au/TiO_2 is consistent with the widely accepted stepwise proton-electron transfer (SPET) mechanism[32,49,50], where water readily deprotonates on TiO_2 before being oxidized by the photogenerated hole, making the electron transfer step ($OH^- + h^+ \rightarrow$ •OH) the RDS. Conversely, the large KIE for Au/TiO_2@pSiO_2–1.7 suggests that molecular water confined in the nanopores acts directly as the hole acceptor, generating •OH radicals through a concerted proton-electron transfer (CPET) pathway ($H_2O + h^+ \rightarrow$ •OH + H^+). As a result, the slower dissociation and deuteron transfer in D_2O compared to H_2O greatly reduce the •OH radical production.

At a molecular level, this mechanistic divergence stems from the preferential reactivity of photogenerated holes with either molecular water or hydroxide anions (OH^-). The SPET mechanism on Au/TiO_2 suggests extensive water dissociation, populating the surface with OH^- that are highly reactive toward holes. In contrast, the shift to a CPET mechanism in Au/TiO_2@pSiO_2–1.7 indicates that confined water resists dissociation, reacting instead in its molecular form. This change can be attributed to the weakened HB network and reduced solvation effect within the nanopores[26,32]. The elevated •OH production over Au/TiO_2@pSiO_2–1.7 suggests that the CPET mechanism provides a more effective route for generating the •OH radicals necessary for CH_4 activation than the two-step SPET pathway. Thus, confinement-driven changes in water reactivity and PCET pathways are key to enhanced CH_4 conversion for Au/TiO_2@pSiO_2–1.7.

As the WOR-producing •OH is key to CH_4 activation, its KIE influences the KIE of overall CH_4 oxidation. Consequently, Au/TiO_2 does not show KIE effect for CH_4 conversion, and Au/TiO_2@pSiO_2-1.7 shows KIE value of 1.3–1.6 (Fig. 6b, Supplementary Figs. 61–64). The KIE decreases over time for Au/TiO_2@pSiO_2–1.7, likely due to H/D exchange between CH_4 and D_2O during reactions (Supplementary Fig. 64, Supplementary Note 5).

On the ORR side, a large KIE of 2.97 is also observed for Au/TiO_2@pSiO_2–1.7 (Fig. 6c), which is expected for the 2e⁻ process that produces H_2O_2 from oxygen and proton. In stark contrast, a reverse KIE for H_2O_2 production was observed over Au/TiO_2, indicating that the confined water significantly modulates the PT and ET dynamics. Notably, the observed shift in ORR pathway from the 1e⁻ process for Au/TiO_2 to the 2e⁻ process for Au/TiO_2@pSiO_2 can also be attributed to facilitated proton transfer due to water confinement. Compared to the 1e⁻ process, the 2e⁻ process is thermodynamically more viable but requires simultaneous transfer of two protons. Therefore, efficient proton transfer, along with increased protons generated from the enhanced WOR process, is responsible for the shift to the 2e⁻ process and enables efficient production of H_2O_2.

Confined water characterization

The weakened HB network of the confined water was analyzed by in situ diffuse reflectance infrared Fourier transform spectroscopy (DRIFTS) measurement at various relative humidity (RH) levels (Fig. 6d–g, Supplementary Figs. 65, 66). The broad OH stretching band (2800–3600 cm^{-1}) is sensitive to the HB network configuration and can be deconvoluted into distinct Gaussian sub-bands (Fig. 6f)[31,34]. From Au/TiO_2 to Au/TiO_2@pSiO_2-1.7, water in the smaller pore shows a significantly larger portion of DA to DDAA ratio along with a lower average number of HBs (<N_{HB}>) (Fig. 6g, Supplementary Table 9), indicating a weakened HB network. A similar trend was observed in the HOH bending (1500–1800 cm^{-1}) region (Fig. 6e), where deconvolution of the spectra can give the ratio between two peaks at 1620 cm^{-1} and 1680 cm^{-1}, attributed to DA and DDAA water clusters[31]. These results suggest that H_2O molecules within smaller pores adopt a more linear arrangement with a weaker HB network, leading to more isolated water species that are prone to oxidation and a reduced solvation that better stabilizes the semi-hydrophobic •OH radicals.

To rationalize the role of water structure, we performed MD simulations using MLPs on the anatase TiO_2(101) surface[44,51]. Two different water environments were modeled: one containing 128 water molecules to represent the bulk system and the other with an interfacial layer of 39 molecules designed to mimic the restricted content of the confined system within the 1.7 nm pores (Supplementary Fig. 67a–c, Supplementary Data 1). Simulated water structures yielded DA/DDAA ratios in reasonable agreement with the experimental DRIFTS data (Fig. 6g, Supplementary Fig. 67d), supporting the qualitative consistency of our computational model. Using this framework, we computed the energetics of the SPET and CPET pathways, corresponding to the oxidation of surface hydroxide (*OH_t^-, reactions (1)–(3)) and adsorbed molecular water (*H_2O_{ad}, reaction (4)), respectively (Supplementary Fig. 68, Supplementary Data 1)[49].

Although the reaction barriers for hole-driven oxidation are low under standard conditions (barrierless for *OH^-; ~12.5 kJ/mol for *H_2O), the reaction rate is governed by the extremely low concentration of surface-reaching holes ($C_{h+} = 10^{-9}$ monolayer (ML)) under realistic photocatalytic conditions[49,50,52,53]. To account for this, we converted this concentration constraint into an equivalent energetic penalty, which adds an additional barrier of ~51.3 kJ/mol to the hole-involving steps (Supplementary Note 6). In bulk water, exergonic dissociation (−5.2 kJ/mol) populates the surface with *OH_t^-, resulting in a lower effective barrier for SPET (46.1 kJ/mol) compared to CPET (63.8 kJ/mol) (Fig. 6h, Supplementary Figs. 69, 70). Under confinement, however, water dissociation becomes unfavorable (20.3 kJ/mol), which stabilizes molecular *H_2O (Fig. 6i, Supplementary Figs. 69, 70). This raises the effective barrier of SPET to 71.6 kJ/mol, thereby shifting the reaction to the CPET pathway. This mechanistic distinction is robust across a wide range of hole concentrations, even at a concentration of 10^{-4} ML (Supplementary Fig. 71). These computational findings align well with our experimental KIE results.

Furthermore, the nanoconfined environment enhances the stability of the generated •OH radicals. In bulk water, •OH radical is prone to deprotonation to form surface oxygen radicals (•O_t^-) through reaction (5) (Supplementary Fig. 68)[53], a process with a barrier (45.2 kJ/mol) slightly lower than that of radical production, facilitating rapid consumption (Fig. 6h). However, the disrupted hydrogen-bond network in the confined system hinders this process. Quantitative analysis shows a substantial increase in both the free energy and activation barrier for this step, rising from ~45 kJ/mol in bulk to >60 kJ/mol under confinement (Fig. 6i). This suggests that the deprotonation barrier exceeds the •OH production barrier in nanopores, potentially extending the lifetime of semi-hydrophobic •OH species and facilitating their participation in CH_4 activation.

Therefore, both enhanced methane conversion and H_2O_2 production of the Au/TiO_2@pSiO_2 can be explained by the weakened HB network of the confined water in porous silica (Fig. 7): (a) for h^+ driven WOR, confined water with disrupted HB networks suppresses dissociation and preferentially reacts with h^+ in its molecular form, causing a shift from SPET to CPET mechanism that generates more •OH radical for CH_4 activation; (b) for e^- driven ORR, confined water with

https://doi.org/10.1038/s41467-026-69719-z

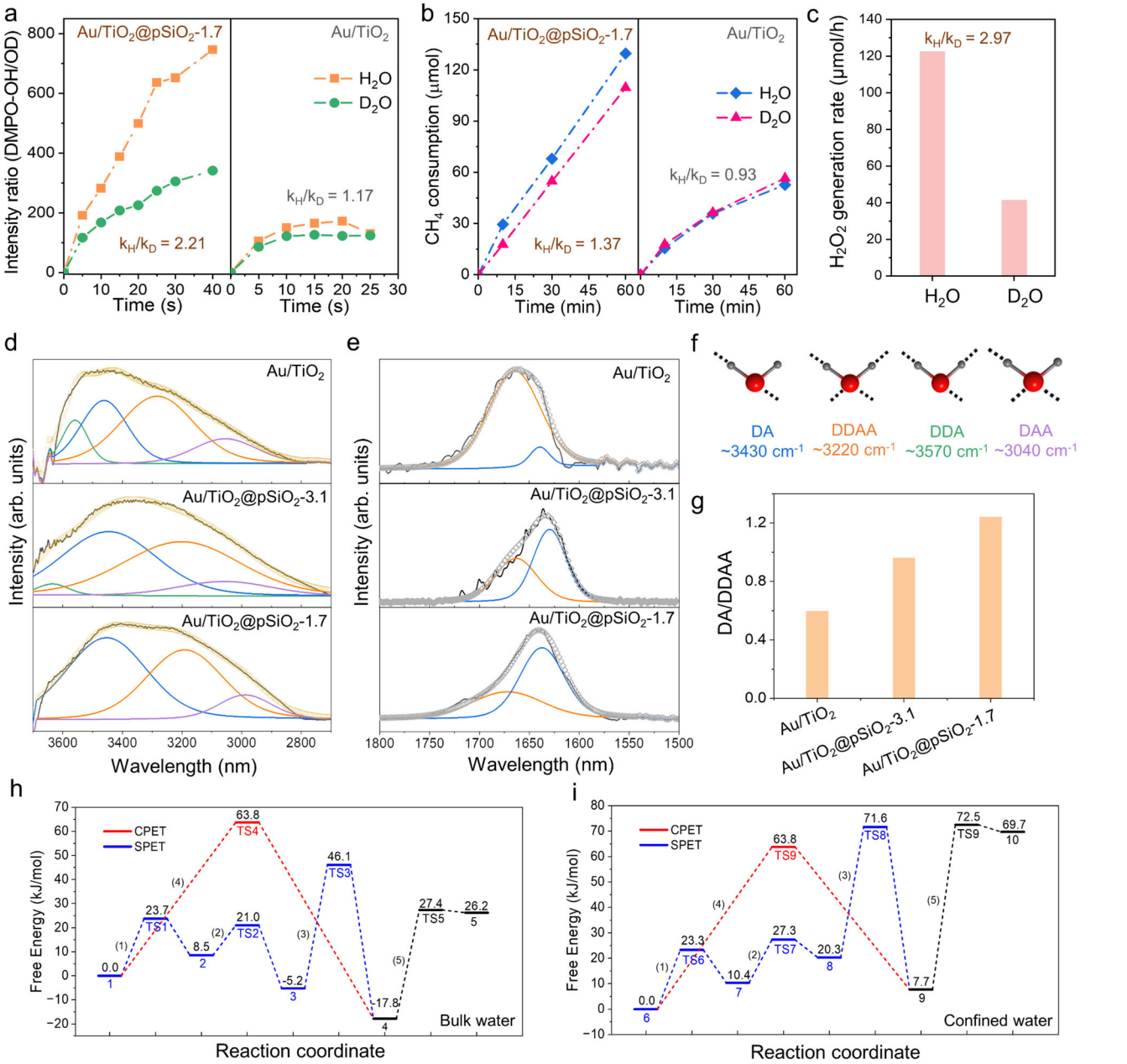

Fig. 6 | H/D KIE and in situ DRIFTS studies over Au/TiO_2@pSiO_2 catalysts. **a** Comparison in •OH radical production over Au/TiO_2 and Au/TiO_2@pSiO_2-1.7 measured in H_2O and D_2O. **b** Comparison in CH_4 conversion rate over Au/TiO_2 and Au/TiO_2@pSiO_2-1.7 measured in H_2O and D_2O. **c** Comparison in H_2O_2 generation rate over Au/TiO_2 and Au/TiO_2@pSiO_2-1.7 measured in H_2O and D_2O. **d** DRIFTS analysis of the OH stretching band of the water in different photocatalysts. **e** DRIFTS analysis of the HOH bending band of the water in different photocatalysts. In (**d**, **e**), colored curves represent the deconvoluted components of specific HB environments (blue: DA; orange: DDAA; green: DDA; purple: DAA); The black lines denote the raw data, while the hollow circles (yellow in (**d**), gray in (**e**)) represent the cumulative fitted curves. **f** Spectroscopically observable hydrogen-bonding configurations of H_2O. **g** Mean HB state of water in Au/TiO_2 and Au/TiO_2@pSiO_2-X samples derived from DRIFTS. Dashed lines represent hydrogen bonds between O (red) and H (gray). **h** Free energy profiles for water dissociation and •OH generation/deprotonation on the anatase TiO_2(101) surface in bulk water. **i** Corresponding free energy profiles in confined water. Both energy profiles (**h**, **i**) were calculated assuming a hole concentration of $C_{h+} = 10^{-9}$ ML.

weakened HB transfers proton more efficiently, enabling a shift from $1e^-$ to $2e^-$ process that directly produces H_2O_2.

Discussion

In summary, we have demonstrated a core-shell photocatalyst design that leverages spatial confinement to modulate water structure, leading to a significant enhancement in both CH_4 conversion and H_2O_2 production. The confined water with weaker HB networks significantly modulates the PT and ET dynamics in the reaction involving photogenerated electrons and holes. Specifically, the confined water suppresses dissociation and preferentially reacts with h^+ in WOR, causing a shift from SPET to CPET mechanism and generating more •OH radicals to activate CH_4. Concurrently, the weakened HB network facilitates more efficient proton transfer in ORR, enabling a shift from the $1e^-$ to the $2e^-$ process and directly producing H_2O_2. This study provides a fundamental understanding of how interfacial water structure can be engineered to optimize photocatalytic performance, opening new avenues for photocatalyst design.

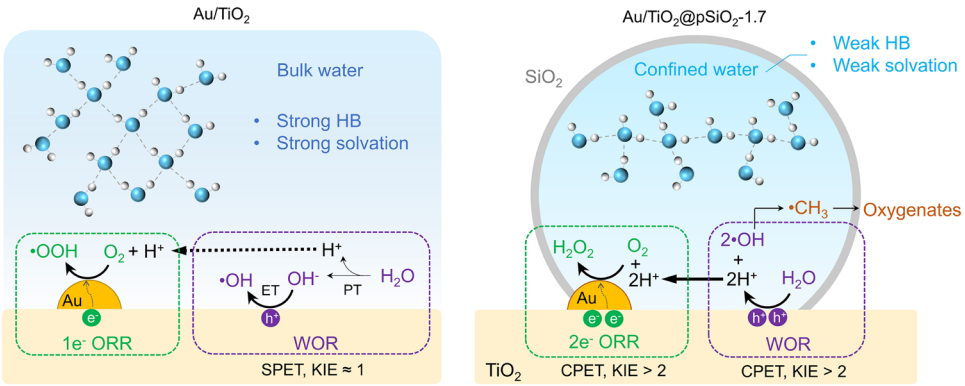

Fig. 7 | Proposed mechanistic pathways and the role of confined water. The schematic illustrates the distinct PCET pathways over Au/TiO_2 in bulk water (left) versus Au/TiO_2@pSiO_2-1.7 with confined water (right). Over Au/TiO_2, water oxidation to •OH radical proceeds via SPET, and O_2 reduction follows a $1e^-$ pathway; In contrast, the confined water with disrupted HB networks promotes the CPET pathway for water oxidation to •OH radicals and $2e^-$ pathway for O_2 reduction. H atom: light gray; O atom: ice blue.

Methods

Materials

All reagents were commercially obtained without purification. Titanium dioxide (P25, ≥99.5%), gold (III) chloride trihydrate ($HAuCl_3$•$3H_2O$, 99.99%), chloroplatinic acid (H_2PtCl_6, ≥99.5%), palladium chloride ($PdCl_2$, 99.9%), and Sodium sulfate (Na_2SO_4, ≥99%) were purchased from Sigma Aldrich. Rhodium(III) chloride trihydrate ($RhCl_3$•$3H_2O$, 98%), methyltrimethoxysilane (98%), dodecyltrimethylammonium bromide (C_{12}TAB, ≥99%), cetyltrimethylammonium bromide (C_{16}TAB, ≥99%), n-hexane (95%), tetraethyl silicate (TEOS, ≥99%), ammonium acetate (≥99%), coumarin (≥98%), 7-hydroxycoumarin (≥99%), acetylacetone (≥99.5 %), benzoic acid (≥99%), deuterium water (≥99.9atom%), $H_2{}^{18}O$ (≥97%), hydroxybenzoic acid (≥99%), 5,5-dimethyl-1-pyrrolidinium N-oxide (DMPO, ≥97%), Tetra-methylpiperidine N-oxide (TEMPO, ≥99%) were purchased from Aladdin. Ammonium hydroxide (NH_3•H_2O, 25–28%), dimethyl sulfoxide (≥99.9%), ethanol (99%), sodium borohydride ($NaBH_4$, 98%), sodium iodate ($NaIO_3$, 99.8%), ammonium oxalate ($(NH_4)_2C_2O_4$, 99.5%) and salicylic acid (HOC_6H_4COOH, 99%) were purchased from Sinopharm Chemical Reagent Co., Ltd., China. The Ag/AgCl electrode was purchased from Shanghai Chenhua.

Preparation of M/TiO_2 photocatalyst

Metal cocatalyst (Au, Pt, Pd, Rh) was loaded onto TiO_2 (P25) using a simple $NaBH_4$ reduction method[9,38]. Typically, 50 mg of TiO_2 was ultrasonically dispersed in 30 mL of deionized water, after which a specific amount of metal precursor solution ($HAuCl_3$•$3H_2O$, H_2PtCl_6, $PdCl_2$, $RhCl_3$•$3H_2O$) was added. Following 10 min of stirring, 2 mL of freshly prepared 0.1 M $NaBH_4$ was added. After an additional 30 min of stirring, the product was collected by centrifugation, washed with deionized water, and dried in an oven at 60 °C. The metal loadings for the catalyst are 0.1 wt%, unless specifically noted.

Preparation of M/TiO_2@pSiO_2-X

To synthesize M/TiO_2@pSiO_2-1.7 (M denoted to Au, Pd, Pt, Rh), 100 mg of C_{12}TAB was used as the templating agent, which was dissolved in 10 mL of deionized water and 40 mL of anhydrous ethanol. Subsequently, 50 mg of M/TiO_2 was added, sonicated for 30 mins, followed by the addition of TEOS. After 15 min of stirring, 0.5 mL ammonium hydroxide solution (25–28%) was added, and the mixture was stirred overnight. The product was collected via centrifugation, washed twice with DI H_2O and ethanol, dried at 60 °C, and calcined at 550 °C for 2 h in static air to remove the C_{12}TAB templates. TEOS volume controlled the SiO_2 thickness; 300 µL produced an 8 nm SiO_2 shell. For the M/TiO_2@pSiO_2-2.6 sample, the synthesis process was identical, except C_{16}TAB was used as the template. The preparation of M/TiO_2@pSiO_2-3.1 followed the same procedure as M/TiO_2@pSiO_2-2.6, with the exception that 10 mL of n-hexane was added to the mixture prior to the addition of TEOS. The metal loadings for the catalysts are 0.1 wt%, unless specifically noted.

Preparation of TiO_2@pSiO_2 and TiO_2@pSiO_2-Au

The synthesis procedure for TiO_2@pSiO_2 was the same as the synthesis of M/TiO_2@pSiO_2 except using TiO_2 as the starting material. The synthesis procedure for TiO_2@pSiO_2-Au was the same as the synthesis of Au/TiO_2, except using TiO_2@pSiO_2 as the supporting material.

Hydrophobic modification of Au/TiO_2@pSiO_2-1.7

The Au/TiO_2@pSiO_2-1.7 catalyst (50 mg) was ultrasonically dispersed in 30 mL of n-hexane, followed by the addition of methyltrimethoxysilane (MTMS) at varying mass ratios (y wt% relative to the catalyst's mass). The resulting suspension was ultrasonicated for 2 h and subsequently stirred at room temperature for 24 h. The solid product was then collected by centrifuge, washed sequentially with n-hexane (three times) and anhydrous ethanol (three times), and dried at 80 °C. The obtained catalyst was denoted as Au/TiO_2@pSiO_2-y wt% MTMS. The y wt% is the added MTMS amount; the actual MTMS loading should be lower.

Characterization

The crystal structure of the catalysts was characterized using a powder X-ray diffractometer D2 (Bruker, Switzerland) with Cu Kα radiation (λ = 1.542 Å). Morphologies of the photocatalysts were studied using TEM (JEM-1400plus) and scanning electron microscopy (SEM, JEOL JEM-7800F). High-resolution TEM (HRTEM) images, HAADF-STEM images, and corresponding EDS maps were collected using a JEOL JEM-F200 field-emission microscope operated at 200 kV. Nitrogen sorption isotherms were collected on a BELSORP-Max 2 apparatus. The metal loading in the photocatalysts was determined by an inductively coupled plasma optical emission spectrometer (ICP-OES, Icap7400, Thermo). UV-Vis DRS were recorded on a Cary 5000 spectrometer (Agilent) equipped with an integrating sphere. The absorption spectra were obtained using the Kubelka–Munk transformation. XPS were collected using a Thermo Fisher ESCALAB 250Xi spectrometer with monochromatic Al-Kα X-rays as the excitation source. All spectra were calibrated to the C 1 s peak at 284.8 eV. In-situ XPS spectra were measured at BL02B01 in the Shanghai Synchrotron Radiation Facility (SSRF), where the data were collected under dark or during irradiation. All spectra were calibrated to an Au foil. The hydrophobicity of the as-prepared catalyst was measured using a contact angle goniometer (SL200KS).

Steady-state PL spectra were recorded on the Horiba Fluorolog-3 Spectrometer with an excitation wavelength of 350 nm. Time-resolved PL spectra were measured on the same instrument with an excitation wavelength of 367 nm. All electrochemical measurements (photocurrent, EIS, and Mott-Schottky tests) were performed on a Gamry Instrument Interface 1010E workstation using a three-electrode system. A 1 M Na_2SO_4 solution (pH = 6.8 ± 0.1) served as electrolyte, with Ag/AgCl (3 M KCl) as the reference electrode, platinum plate as the counter electrode and catalysts loaded on indium-tin oxide (ITO) as the working electrode. Automatic iR compensation was applied for Mott-Schottky measurements.

The solution resistance (R_s) was determined via EIS at open-circuit potential (100 kHz −3 Hz, 10 mV amplitude). The high-frequency intercept of the Nyquist plot yielded an average R_s of 19.2 ± 0.2 Ω. All potentials in this work are converted to the RHE scale by E (vs RHE) = E (vs Ag/AgCl) + 0.210 V + 0.0591 × pH.

Photocatalytic activity measurements

Evaluation of photocatalytic activity for CH_4 oxidation was performed using a high-pressure autoclave (250 mL) with an optical sapphire window. After ultrasonically dispersing the catalyst (10 mg) in deionized water (100 mL) for 30 min, the reactor was purged with argon (99.999%). The gaseous reactants, CH_4 (99.999%) and O_2 (99.999%), were subsequently introduced into the vessel at partial pressures of 2.5 MPa and 1.0 MPa, respectively. The reactor was irradiated from the top using an LED lamp (365 nm, PLS-LED100C, Beijing Perfectlight Technology Co., Ltd.). The photocatalytic reaction was conducted for 1 h at 25 °C. A thermocouple was inserted into the solution to directly detect the temperature of the solution. The photoreactor was directly connected to a gas chromatograph (Agilent GC 8890) equipped with a flame ionization detector (FID) and a methanizer for the gas product analysis of CO_2 and ethane. The liquid products (CH_3OOH, CH_3OH, and HCOOH) were analyzed by ^{1}H-NMR (Bruker 400 MHz), with DMSO added as an internal standard.

HCHO quantification

The amount of HCHO was quantified using the acetylacetone color-development method[37,54]. Typically, 0.5 mL of the sample liquor, 2 mL of deionized water and 0.5 mL of reagent solution (consisting of 15 g of ammonium acetate, 0.3 mL of acetic acid, and 0.2 mL of acetylacetone dissolved in 100 mL of H_2O) were mixed and placed in a water bath at 35 °C for 40 min. The absorption value of the mixture at 412 nm was then measured using UV-visible absorption spectroscopy (PerkinElmer, Lambda 265).

H_2O_2 quantification

The concentration of produced H_2O_2 was determined using the titanium oxalate spectrophotometric method[55]. To prepare the test solution, 0.636 g of potassium titanium oxalate and 0.02 mL of concentrated sulfuric acid were dissolved in 99.98 mL of DI H_2O. Then, 1 mL of the above test solution was mixed with 1 mL of the reaction sample. The absorption of the mixture was measured at 390 nm using UV-visible absorption spectroscopy (PerkinElmer, Lambda 265).

CH_4 conversion rates and oxygenates selectivity calculation

The methane conversion and oxygenates selectivity in this process are calculated according to the following equations:

$$Conversion(CH_4) = \frac{mol_{total\,formed\,products}}{mol_{initial\,methane}} \times 100\%$$

$$Oxygenates\,selectivity = \frac{mol_{produced\,CH_3OH,\,CH_3OOH,\,HCHO\,and\,HCOOH}}{mol_{total\,formed\,products}} \times 100\%$$

The initial methane amount in the system is calculated according to the following equation (V is the volume of the headspace of the reactor):

$$Initial\,methane\,(\mathrm{mol}) = \frac{P_{methane} \times V}{\mathrm{R} \times T\,(298\mathrm{K})}$$

AQY of CH_4 conversion was calculated according to the following equation:

$$AQY = \frac{N(electrons)}{N(photons)} \times 100\%$$

where *N(electrons)* and *N(photons)* represent the number of reacted electrons and the number of incident photons, respectively. *N(photons)* = *IAt/E*, where *I*, *A*, *t* and *E* represent incident light intensity (W/cm^2), irradiation area (cm^2), light incident time (s) and photo energy (J), respectively. *N(electrons)* was calculated based on the following reported work[9,20]: $N(electrons) = n(CH_3OOH) + 3n(CH_3OH) + 5n(HCHO) + 7n(HCOOH) + 9n(CO_2)$, where $n(CH_3OOH)$, $n(CH_3OH)$, $n(HCHO)$, $n(HCOOH)$ and $n(CO_2)$ represent the number of moles of produced CH_3OOH, CH_3OH, HCHO, HCOOH and CO_2, respectively. The AQY for H_2O_2 production is calculated similarly, with $N(electrons) = 2n(H_2O_2)$, where $n(H_2O_2)$ represents the number of moles of H_2O_2 produced. The light intensity was calibrated using a PL-MW2000 optical power meter (Beijing Perfectlight Technology Co., Ltd.). Error bars represent the standard deviation (SD) from three independent experiments. Data points without error bars represent single measurements.

Catalyst cycling test

To study the reusability of the catalyst, the solid catalyst was separated by centrifugation after each reaction run. The catalysts were re-used in the next run after drying at 90 °C overnight under vacuum and annealing at 300 °C in air to remove any adsorbed organic species. Aq

CH_4-TPD experiments

CH_4-TPD were performed using a Chemisorption analyzer (ChemStar). Catalysts were pretreated at 150 °C for 30 min under a He flow of 30 sccm. After cooling to 50 °C, adsorption was conducted under a pure CH_4 atmosphere for 120 min. The sample was then purged with He for 30 min, and the TPD profile was recorded at a heating rate of 5 °C/min under a He flow.

Analysis of photogenerated •OH radicals

The •OH production was measured using PL with coumarin, which reacts with •OH to form fluorescent 7-hydroxycoumarin (7-HC) (Supplementary Fig. 48). 2 mg catalyst was dispersed in 100 mL of 1.0 mM coumarin solution in the dark, irradiated for 10 min, then centrifuged and analyzed with a Horiba FluoroLog-3 spectrofluorometer at 332 nm excitation.

Isotope experiments for identifying the origin of products

For carbon source investigation with isotopically labeled $^{13}CH_4$: 10 mg $Au/TiO_2@pSiO_2$ was dispersed in 5 mL H_2O, and the reactor was purged with Ar to remove air. The photoreactor was then filled with 0.55 MPa $^{13}CH_4$ (99%), 0.45 MPa $^{12}CH_4$ (99.999%) and 0.2 MPa O_2 (99.999%). After 2 h of light irradiation, gas products were analyzed by gas chromatograph-mass spectroscopy (GC-MS, Shimadzu), and liquid products by ^{1}H-NMR.

For oxygen source investigation with ^{18}O isotope labeling with $^{18}O_2$/$H_2{}^{16}O$ and $^{16}O_2$/$H_2{}^{18}O$: 10 mg $Au/TiO_2@pSiO_2$ was dispersed in 10 mL $H_2{}^{16}O$ or ($H_2{}^{18}O$), and the reactor was purged with Ar. The photoreactor was charged with 2.5 MPa CH_4 (99.999%) and 0.5 MPa $^{18}O_2$ (98%) (or $^{16}O_2$). Products were analyzed by GC-MS after 2 h of light irradiation.

EPR measurements

In situ electron paramagnetic resonance (EPR) spectra were acquired using a Bruker ESR5000 spectrometer equipped with a 300 W xenon lamp (PLS-SXE300 + /UV, Perfectlight) for illumination. 5,5-Dimethyl-1-pyrroline-N-oxide (DMPO) served as the radical trap. For •OH radical detection, 5 mg of catalyst was dispersed in 5 mL of distilled H_2O in the dark and purged with ultrapure argon (99.999 vol.%) for 2 min. For •OOH radical detection, 5 mg of catalyst was dispersed into a 5 mL of DMSO with O_2 bubbling for 2 min.

Investigation of the photochemical pathway of H_2O_2 production

To determine if H_2O_2 production originates from WOR or ORR, liquid samples from $^{18}O_2$ or $H_2{}^{18}O$ isotope CH_4 oxidation experiments were analyzed. As shown in Supplementary Fig. 55, 2 mL of the liquid samples was injected into a sealed vial (Vial A) and purged with He for 30 min. Another vial (Vial B), containing 200 mg of MnO_2 and 5 mL H_2O, was also purged with He for 30 min. Then, 2 mL from Vial A was injected into Vial B. After complete decomposition of H_2O_2 over MnO_2, 1 mL of gas from the headspace of Vial B was extracted for GC-MS analysis.

Investigation of the photochemical pathway for •OH generation

To analyze photochemical pathways of •OH production,$^{18}O_2$ isotope experiments and $H_2{}^{18}O$ isotope experiments were conducted. In the $^{18}O_2$ experiments, 2 mg of catalyst was dispersed in 1 mL of 1 mM benzoic acid solution ($H_2{}^{16}O$ as solvent). The reactor was purged with Ar to remove air and filled with 0.1 MPa $^{18}O_2$ (98%). The reaction was carried out under UV irradiation for 600 s. The products were analyzed by liquid chromatography–mass spectrometry (LC–MS, Thermofisher). Similarly, for the $H_2{}^{18}O$ isotope experiments, the setup was identical except using benzoic acid dissolved in $H_2{}^{18}O$ and 0.1 MPa $^{16}O_2$.

KIE measurements

For •OH radical generation, 5 mg of catalyst were dispersed in 2 mL of either D_2O or H_2O, and in situ EPR measurements were performed to track the formation of •OH radicals. For CH_4 conversion, 10 mg of catalysts were dispersed in 10 mL of D_2O or H_2O. The reactor vessel was then pressured to 2.5 MPa CH_4 and 1 MPa of O_2, followed by light irradiation, and liquid products were collected at specific time intervals for analysis. For H_2O_2 generation, 10 mg of catalysts were dispersed in 10 mL of D_2O or H_2O. The reactor vessel was then pressured to 1 MPa of O_2, followed by light irradiation. The resulting liquid product was collected for analysis.

Active species scavenging experiments

The experiments were conducted by adding different types of radical scavengers was used to understand the role of radical species involved in the photocatalytic CH_4 oxidation. Tetramethylpiperidine N-oxide (TEMPO) as a scavenger for all radicals, and ammonium oxalate ($(NH_4)_2C_2O_4$), sodium iodate ($NaIO_3$), salicylic acid (HOC_6H_4COOH) as scavengers for photogenerated holes, photogenerated electrons, hydroxyl radicals, respectively[15]. In a typical experiment, 10 mg photocatalyst was dispersed in 100 mL distilled water containing 1 mmol radical scavengers. After being finely sealed, the suspension was purged with ultrapure Ar (99.999%) for 20 min to completely remove air. Then O_2 (99.999%) and CH_4 (99.999%) were injected to acquire the desired pressure. The reaction was conducted for 10 mins. Products including CH_3OH, CH_3OOH, HCHO, HCOOH and CO_2 were measured according to the method shown above.

In situ DRIFTS measurements

In situ DRIFTS measurements were performed using a Thermo Scientific iS50 FTIR spectrometer equipped with a liquid-nitrogen-cooled MCT/A detector. An infrared cell (Harrick) with ZnSe windows was used for measurements. Each spectrum was recorded by averaging 64 scans at a resolution of 4 cm^{-1}. Samples were first pretreated at 673 K (5 K min^{-1}) for 30 min in flowing O_2 (20 mL min^{-1}) to remove impurities adsorbed on the surface. Background spectra were then taken at 303 K in dry Ar. Wet Ar (Ar/H_2O with controlled humidity) was subsequently introduced (20 mL min^{-1}), and spectra were acquired at the 303 K. By using the following equation proposed by previous work[31,34], we determined the average number of hydrogen bonds of each water molecule:

$$< N_{HB} > = 4 \times A_{DDAA} + 3 \times A_{DDA} + 3 \times A_{DAA} + 2 \times A_{DA}$$

MLP-MD simulations

All MD simulations were conducted using LAMMPS[56] with an implementation of an MLP trained on the optB88-vdW density functional, which accurately captures the energetics and dynamics of water dissociation on TiO_2 surfaces. This approach, developed by Zeng et al[51], enables large-scale simulations of water-TiO_2 interfaces with near DFT accuracy. As MLPs are trained on DFT data, they suffer from the same limitations as DFT[57]. A timestep of 1 fs was used for all simulations. Free-energy landscapes at 300 K were evaluated using metadynamics, as implemented in LAMMPS patched with PLUMED[49]. Metadynamics simulations were performed to explore the free-energy surfaces associated with •OH generation and subsequent transformations. The PLUMED input file specifying the collective variables (CVs) is provided in Supplementary Table 10. All simulations were carried out in the NVT ensemble using a Nosé-Hoover thermostat. Each independent metadynamics trajectory was run for 20 ns. Following G. Bussi et al[58], we obtained the average 1D free energy profile after t_{fill} that all the free energy minima are filled with Gaussian hills, and then computed the values of the free energy barrier and reaction free energy. According to the free energy barrier and reaction free energy curves shown in Fig. 6h, i, Supplementary Fig. 71, we determined the t_{fill} as 10 ns for these simulations.

Structure of Water/Anatase TiO_2 (101) interface in MD simulations

The anatase TiO_2(101) surface exhibits a terraced morphology characterized by step-edge twofold-coordinated oxygen atoms (O_{2c}), which is critical for proton transfer, and fivefold-coordinated titanium sites (Ti_{5c}) for water adsorption. The slab size of $p(1 \times 3)$ TiO_2(101) surface is 10.5 Å × 11.5 Å × 48.6 Å (Supplementary Fig. 67). This surface was represented using a ten-trilayer O-Ti-O slab comprising 180 atoms, a thickness validated to eliminate slab-size artifacts in surface energetics and water adsorption behavior. To mimic the bulk water environment surrounding Au/TiO_2, a cell containing 128 water molecules was constructed, corresponding to a density of 1 g cm^{-3}. To model the confined water for Au/TiO_2@pSiO_2-1.7, a system with 39 water molecules, corresponding to a three-layer hydration film with reduced water content, was constrained at the interface between the TiO_2(101) surface and a virtual silica pore wall. The HB network of water molecules was analyzed using a workflow developed on top of the MD Analysis toolkit[59]. For each trajectory snapshot, the HB topology was determined by first assigning to each oxygen atom its two nearest hydrogen atoms. The remaining hydrogen atom in each water molecule was subsequently associated with the nearest oxygen atom based on the shortest O–H distance. HBs were identified using standard geometric criteria, namely an O_1–O_2 distance of <3.0 Å and an O_1–H_2 distance of <2.5 Å, where subscripts 1 and 2 refer to atoms belonging to the hydrogen-bond acceptor and donor, respectively. Interfacial hydrogen bonds were quantified using a donor-acceptor distance cutoff of 3.0 Å together with an angular cutoff of 30°, following established protocols[60].

Data availability

All the data that support the findings of this study are included within the article and its Supplementary Information files. Source data are provided with this paper.

References

1. Maeda, K. & Domen, K. Photocatalytic water splitting: recent progress and future challenges. *J. Phys. Chem. Lett.* **1**, 2655–2661 (2010).
2. Li, K., Peng, B. & Peng, T. Recent advances in heterogeneous photocatalytic CO_2 conversion to solar fuels. *ACS Catal.* **6**, 7485–7527 (2016).
3. Chong, M. N., Jin, B., Chow, C. W. K. & Saint, C. Recent developments in photocatalytic water treatment technology: A review. *Water Res.* **44**, 2997–3027 (2010).
4. Chen, C., Shi, T., Chang, W. & Zhao, J. Essential roles of proton transfer in photocatalytic redox reactions. *ChemCatChem* **7**, 724–731 (2015).
5. Teng, Z. et al. Atomically dispersed low-valent Au boosts photocatalytic hydroxyl radical production. *Nat. Chem.* **16**, 1250–1260 (2024).
6. Li, X., Wang, C. & Tang, J. Methane transformation by photocatalysis. *Nat. Rev. Mater.* **7**, 617–632 (2022).
7. Li, Q., Ouyang, Y., Li, H., Wang, L. & Zeng, J. Photocatalytic conversion of methane: recent advancements and prospects. *Angew. Chem. Int. Ed.* **61**, e202108069 (2022).
8. Wang, P., Shi, R., Zhao, J. & Zhang, T. Photodriven methane conversion on transition metal oxide catalyst: recent progress and prospects. *Adv. Sci.* **11**, 2305471 (2024).
9. Song, H. et al. Direct and selective photocatalytic oxidation of CH4 to oxygenates with O2 on cocatalysts/ZnO at room temperature in water. *J. Am. Chem. Soc.* **141**, 20507–20515 (2019).
10. Latimer, A. A., Kakekhani, A., Kulkarni, A. R. & Nørskov, J. K. Direct methane to methanol: the selectivity–conversion limit and design strategies. *ACS Catal.* **8**, 6894–6907 (2018).
11. Jiang, Y. et al. Elevating Photooxidation Of Methane To Formaldehyde via TiO_2 crystal phase engineering. *J. Am. Chem. Soc.* **144**, 15977–15987 (2022).
12. Feng, N. et al. Efficient and selective photocatalytic CH4 conversion to CH3OH with O2 by controlling overoxidation on TiO2. *Nat. Commun.* **12**, 4652 (2021).
13. Han, C. et al. Selective cleavage of chemical bonds in targeted intermediates for highly selective photooxidation of methane to methanol. *J. Am. Chem. Soc.* **145**, 8609–8620 (2023).
14. Jiang, Y. et al. Enabling specific photocatalytic methane oxidation by controlling free radical type. *J. Am. Chem. Soc.* **145**, 2698–2707 (2023).
15. Luo, L. et al. Binary Au–Cu reaction sites decorated ZnO for selective methane oxidation to C1 oxygenates with nearly 100% selectivity at room temperature. *J. Am. Chem. Soc.* **144**, 740–750 (2022).
16. Zheng, K. et al. Room-temperature photooxidation of CH_4 to CH_3OH with nearly 100% selectivity over hetero-ZnO/Fe2O3 porous nanosheets. *J. Am. Chem. Soc.* **144**, 12357–12366 (2022).
17. Zhou, Q. et al. Selective photocatalytic oxidation of methane to methanol by constructing a rapid O_2 conversion pathway over Au–Pd/ZnO. *ACS Catal.* **14**, 955–964 (2024).
18. Gong, H. et al. Selective photocatalytic aerobic oxidation of methane to methyl hydroperoxide by ZnO-loaded single-atomic ruthenium oxide catalyst. *J. Am. Chem. Soc.* **147**, 9134–9146 (2025).
19. Zhai, G. et al. Direct photocatalytic oxidation of methane to formic acid with high selectivity via a concerted proton–electron transfer process. *J. Am. Chem. Soc.* **147**, 2444–2454 (2025).
20. Xie, C. et al. Transport mediating core–shell photocatalyst architecture for selective alkane oxidation. *Nano Lett.* **23**, 2039–2045 (2023).
21. Fan, Y. et al. Selective photocatalytic oxidation of methane by quantum-sized bismuth vanadate. *Nat. Sustain.* **4**, 509–515 (2021).
22. Resasco, D. E., P, C. S., Bin, W. & White, J. L. Interaction of water with zeolites: a review. *Catal. Rev.* **63**, 302–362 (2021).
23. Marcus, R. A. On the theory of oxidation-reduction reactions involving electron transfer. I. *J. Chem. Phys.* **24**, 966–978 (1956).
24. Yao, J. et al. Interfacial hydrogen-bond network regulation tuned water dissociation enables selective chlorination of alkenes. *J. Am. Chem. Soc.* **147**, 8024–8031 (2025).
25. Li, P. et al. Hydrogen bond network connectivity in the electric double layer dominates the kinetic pH effect in hydrogen electrocatalysis on Pt. *Nat. Catal.* **5**, 900–911 (2022).
26. Yang, W. et al. Effect of the hydrogen bond in photoinduced water dissociation: a double-edged sword. *J. Phys. Chem. Lett.* **7**, 603–608 (2016).
27. Chen, X. et al. Revealing the role of interfacial water and key intermediates at ruthenium surfaces in the alkaline hydrogen evolution reaction. *Nat. Commun.* **14**, 5289 (2023).
28. Zhang, H., Gao, J., Raciti, D. & Hall, A. S. Promoting Cu-catalysed CO2 electroreduction to multicarbon products by tuning the activity of H2O. *Nat. Catal.* **6**, 807–817 (2023).
29. Wang, T. et al. Enhancing oxygen reduction electrocatalysis by tuning interfacial hydrogen bonds. *Nat. Catal.* **4**, 753–762 (2021).
30. Dubouis, N. et al. Tuning water reduction through controlled nanoconfinement within an organic liquid matrix. *Nat. Catal.* **3**, 656–663 (2020).
31. Verduci, R. et al. Water structure in the first layers on TiO2: a key factor for boosting solar-driven water-splitting performances. *J. Am. Chem. Soc.* **146**, 18061–18073 (2024).
32. Ren, G., Zhou, M. & Wang, H. Weakened interfacial hydrogen bond connectivity drives selective photocatalytic water oxidation toward H_2O_2 at water/brookite-TiO_2 interface. *J. Am. Chem. Soc.* **146**, 6084–6093 (2024).
33. Ma, X. et al. Hydrogen-bond network promotes water splitting on the TiO_2 surface. *J. Am. Chem. Soc.* **144**, 13565–13573 (2022).
34. Bregante, D. T. et al. The shape of water in zeolites and its impact on epoxidation catalysis. *Nat. Catal.* **4**, 797–808 (2021).
35. Wang, T. et al. Confined water for catalysis: thermodynamic properties and reaction kinetics. *Chem. Rev.* **125**, 1420–1467 (2025).
36. Pascal, T. A., Goddard, W. A. & Jung, Y. Entropy and the driving force for the filling of carbon nanotubes with water. *Proc. Natl. Acad. Sci.* **108**, 11794–11798 (2011).
37. Song, H. et al. Selective photo-oxidation of methane to methanol with oxygen over dual-cocatalyst-modified titanium dioxide. *ACS Catal.* **10**, 14318–14326 (2020).
38. Zhang, X. et al. Selective photocatalytic oxidative ethane dehydrogenation on AuPd nanoparticle-decorated TiO_2. *ACS Appl. Mater. Interfaces* **17**, 14119–14128 (2025).
39. Xie, C. et al. Tandem catalysis for CO_2 hydrogenation to C_2–C_4 hydrocarbons. *Nano Lett.* **17**, 3798–3802 (2017).
40. Tennakoon, A. et al. Catalytic upcycling of high-density polyethylene via a processive mechanism. *Nat. Catal.* **3**, 893–901 (2020).
41. Raman, N. K., Anderson, M. T. & Brinker, C. J. Template-based approaches to the preparation of amorphous, nanoporous silicas. *Chem. Mater.* **8**, 1682–1701 (1996).
42. Tang, K. et al. Hydrophobization engineering of the Air–cathode catalyst for improved oxygen diffusion towards efficient Zinc–air batteries. *Angew. Chem. Int. Ed.* **61**, e202202671 (2022).
43. Jin, Z. et al. Hydrophobic zeolite modification for in situ peroxide formation in methane oxidation to methanol. *Science* **367**, 193–197 (2020).
44. Cao, B. et al. Zeolite encapsulation to enhance interfacial gas availability for photocatalytic hydrogen peroxide production. *Angew. Chem. Int. Ed.* **64**, e202422495 (2025).

45. Cao, X. et al. A photochromic composite with enhanced carrier separation for the photocatalytic activation of benzylic C–H bonds in toluene. *Nat. Catal.* **1**, 704–710 (2018).
46. Zhang, Y. et al. Pivotal role and regulation of proton transfer in water oxidation on hematite photoanodes. *J. Am. Chem. Soc.* **138**, 2705–2711 (2016).
47. Liu, S. et al. Transition from sequential to concerted proton-coupled electron transfer of water oxidation on semiconductor photoanodes. *J. Am. Chem. Soc.* **145**, 23849–23858 (2023).
48. Yu, S. et al. CO2-to-methanol electroconversion on a molecular cobalt catalyst facilitated by acidic cations. *Nat. Catal.* **7**, 1000–1009 (2024).
49. Zhao, W.-N. & Liu, Z.-P. Mechanism and active site of photocatalytic water splitting on titania in aqueous surroundings. *Chem. Sci.* **5**, 2256–2264 (2014).
50. Wang, D., Sheng, T., Chen, J., Wang, H.-F. & Hu, P. Identifying the key obstacle in photocatalytic oxygen evolution on rutile TiO2. *Nat. Catal.* **1**, 291–299 (2018).
51. Zeng, Z. et al. Mechanistic insight into water dissociation on pristine low-index TiO2 surfaces from machine learning molecular dynamics simulations. *Nat. Commun.* **14**, 6131 (2023).
52. Tamaki, Y. et al. Dynamics of efficient electron–hole separation in TiO2 nanoparticles revealed by femtosecond transient absorption spectroscopy under the weak-excitation condition. *Phys. Chem. Chem. Phys.* **9**, 1453–1460 (2007).
53. Li, F., Chen, J.-F., Gong, X.-Q., Hu, P. & Wang, D. Subtle structure matters: the vicinity of surface Ti5c cations alters the photooxidation behaviors of anatase and rutile TiO_2 under aqueous environments. *ACS Catal.* **12**, 8242–8251 (2022).
54. Ding, J. et al. Asymmetrically coordinated cobalt single atom on carbon nitride for highly selective photocatalytic oxidation of CH_4 to CH_3OH. *Chem* **9**, 1017–1035 (2023).
55. Agarwal, N. et al. Aqueous Au-Pd colloids catalyze selective CH4 oxidation to CH3OH with O2 under mild conditions. *Science* **358**, 223–227 (2017).
56. Plimpton, S. Fast parallel algorithms for short-range molecular dynamics. *J. Comput. Phys.* **117**, 1–19 (1995).
57. Cohen, A. J., Mori-Sánchez, P. & Yang, W. Insights into current limitations of density functional theory. *Science* **321**, 792–794 (2008).
58. Bussi, G. & Laio, A. Using metadynamics to explore complex free-energy landscapes. *Nat. Rev. Phys.* **2**, 200–212 (2020).
59. Grimme, S., Ehrlich, S. & Goerigk, L. Effect of the damping function in dispersion corrected density functional theory. *J. Comput. Chem.* **32**, 1456–1465 (2011).
60. Hack, J. H. et al. Structural characterization of protonated water clusters confined in HZSM-5 zeolites. *J. Am. Chem. Soc.* **143**, 10203–10213 (2021).

Acknowledgments

We thank Prof. P. Liu, Prof. Y. Huang, and Prof. P. Hu at ShanghaiTech University for the insightful discussion. We thank Prof. F. Yang and Prof. Y. Yang at ShanghaiTech University for help with FTIR experiments; Dr. S. Chen for help with the EPR measurements; and Prof. G. Ma, Dr. J. Zhang, and Ms. M. Liu for help with photoelectrochemical measurements. This work was financially supported by the Science and Technology Commission of Shanghai Municipality Sailing Program (23YF1426600) and start-up funding from ShanghaiTech University. We thank the Shanghai Synchrotron Radiation Facility of BL02B01 (31124.02.SSRF.BL02B01) for the assistance with in situ XPS measurements. The TEM experiments are supported by the Center for High-resolution Electron Microscopy (C$\hbar$EM) at ShanghaiTech University. We also thank the HPC Platform of ShanghaiTech University for computing time.

Author contributions

C.X. conceived the project. F.L. performed the catalyst preparation, characterization, and catalytic tests. S.W. and B.Y. performed the MD simulations. X.Y.W. performed the HR-TEM, HAADF and EDS characterization. Y.Y. and X.Y.W. helped on TEM image analysis. C.Q. performed the contact angle measurements. X.W. performed XPS experiments. X.L. helped on the in situ XPS experiments. C.X. and F.L. wrote the manuscript. All authors contributed to the data discussion and revision of the manuscript.

Competing interests

The authors declare no competing interests.

Additional information

Supplementary information The online version contains supplementary material available at https://doi.org/10.1038/s41467-026-69719-z.

Correspondence and requests for materials should be addressed to Bo Yang or Chenlu Xie.

Peer review information *Nature Communications* thanks Yuchen Hao and the other anonymous reviewer(s) for their contribution to the peer review of this work. A peer review file is available."